Elucidation and refinement of synthetic receptor mechanisms

Hailey I. Edelstein[1,8], Patrick S. Donahue[1,2,3,8], Joseph J. Muldoon[1,2], Anthony K. Kang[4], Taylor B. Dolberg[1], Lauren M. Battaglia[1], Everett R. Allchin[1], Mihe Hong[1], & Joshua N. Leonard[1,2,5,6,7,*]

[1]Department of Chemical and Biological Engineering, Northwestern University, Evanston, Illinois 60208, United States

[2]Interdisciplinary Biological Sciences Program, Northwestern University, Evanston, Illinois 60208, United States

[3]Medical Scientist Training Program, Northwestern University Feinberg School of Medicine, Chicago, Illinois 60611, United States

[4]Honors Program in Medical Education, Northwestern University Feinberg School of Medicine, Chicago, Illinois 60611, United States

[5]Center for Synthetic Biology, Northwestern University, Evanston, Illinois 60208, United States

[6]Chemistry of Life Processes Institute, Northwestern University, Evanston, Illinois 60208, United States

[7]Member, Robert H. Lurie Comprehensive Cancer Center, Northwestern University, Evanston, Illinois 60208, United States

[8]These authors contributed equally to this work

Contact Information
*Corresponding author: Joshua N. Leonard, j-leonard@northwestern.edu

ABSTRACT

Synthetic receptors are powerful tools for engineering mammalian cell-based devices. These biosensors confer unique capabilities for detecting environmental ligands and transducing signals to control downstream gene expression events such as therapeutic protein production. For many applications, it would be useful to understand how receptor design choices impart desirable performance metrics and trade-offs. Towards this goal, we employed the existing modular extracellular sensor architecture (MESA) and systematically characterized biosensors with previously unexamined protein domain choices. A key finding that might extend to other receptor systems is that choice of transmembrane domain (TMD) is highly consequential. To provide mechanistic insights, we adopted and employed a FRET-based assay to elucidate how TMDs affect receptor complex formation and connected these observations to functional performance. To build further insight into these phenomena, we developed a library of new MESA receptors that sense an expanded set of ligands. Based upon these explorations, we conclude that TMDs affect signaling primarily by modulating intracellular domain geometry, and we apply this understanding to rationally tune receptors. Finally, to guide the design of future receptors, we propose general principles for linking design choices to biophysical mechanisms and performance characteristics.

Keywords: mammalian synthetic biology, receptor engineering, transmembrane domain, biosensor, cell therapy

INTRODUCTION

Engineered cell-based therapies are a promising strategy for the targeted treatment of many diseases (1-4). Central to this approach is the use of genetically encoded sense-and-response programs, which cause the cell to enact a therapeutic function upon detection of specified cues. Designing and implementing a customized functional program requires integrating native and engineered cellular components—including receptors, signal transduction pathways, and genetic regulators—and developing principles and tools for doing so is an active frontier in the field of synthetic biology. Here, we address this need for the subset of strategies that utilize synthetic receptor systems.

Synthetic receptor systems can be designed to interact with or be independent of endogenous signaling (5, 6). One strategy is to couple synthetic receptor-mediated signaling to native pathways such as those involving JAK/STAT, MAPK/ERK, PLCG, PI3K/AKT, NFAT, and mediators downstream of GPCRs (7-10). When paired with downstream engineered promoters, these signals can be redirected to new transcriptional outputs (11, 12) or cell behaviors (13, 14). A second strategy involves using engineered components to redirect the signaling outputs from native receptors via modified phosphorylation (15-18), dimerization (19), or protein recruitment events (20). A third strategy is to circumvent native pathways by using orthogonal systems. For example, synthetic Notch (synNotch) receptors sense surface-bound ligands (21-24), and the modular extracellular sensor architecture (MESA) detects soluble ligands (25-27). Both of these receptor systems regulate endogenous or exogenous genes directly through ligand binding-induced release of a transcription factor (TF). Orthogonal systems are of great interest for cell-based devices, and their intrinsic modularity should facilitate extensions to new ligand inputs and functional outputs (28). Notably, these systems have not been tuned through evolution nor studied deeply in the biological literature, yet their modular structure renders them uniquely suited to iterative improvement. Therefore, there exist unique opportunities for building understanding and improving the performance characteristics of orthogonal synthetic receptors.

This study focuses on exploring and improving MESA receptors (25, 29). The MESA system comprises two receptor chains that dimerize upon ligand binding and release a sequestered TF through proteolytic *trans*-cleavage (**Fig. 1a**). MESA receptors have also been multiplexed to sense multiple ligands (27). Across these studies, we demonstrated that obtaining desirable performance characteristics—low ligand-independent (background) signaling and high fold induction of signaling upon ligand addition—required tuning both the absolute and relative levels at which each receptor chain is expressed. While this phenomenon is not entirely different from what one observes with native receptors and other systems, it would be desirable to minimize this sensitivity to receptor expression level, for example to facilitate translational applications. Moreover, our computational analysis (27) indicated that if design changes could improve the two performance characteristics noted above, this could render biosensor function robust to variations in receptor expression levels. These observations motivate this investigation into refining the MESA design.

In this investigation, we build mechanistic understanding and improve the functional performance of MESA receptors by systematically examining previously unexplored aspects of their design. We identify several tunable receptor handles that improve performance and we employ this knowledge to expand the MESA sensing repertoire and enhance a recently developed MESA receptor that employs a distinct mechanism (26). Finally, we synthesize these observations to propose a framework of biophysically motivated design considerations for building novel synthetic receptors.

MATERIALS AND METHODS

General DNA assembly

Plasmid cloning was performed primarily using standard PCR and restriction enzyme cloning with Vent DNA Polymerase (New England Biolabs (NEB)), *Taq* DNA Polymerase (NEB), Phusion DNA Polymerase (NEB), restriction enzymes (NEB; Thermo Fisher), T4 DNA Ligase (NEB), Antarctic Phosphatase (NEB), and T4 PNK (NEB). Golden gate assembly and Gibson assembly were also utilized. The pBI-EYFP reporter was described previously (Addgene #58855) (25). GBP2-containing and GBP7-containing source plasmids

were a generous gift from Constance Cepko (30). Plasmids were transformed into chemically competent TOP10 *E. coli* (Thermo Fisher) and cells were grown at 37°C.

Cloning MESA receptors

MESA receptors were cloned into pcDNA backbones to confer high expression in HEK293FT cells. These plasmid backbones are versions of the pcDNA3.1/Hygro(+) Mammalian Expression Vector (Thermo Fisher #V87020), modified by our laboratory in previous work (Addgene #138749) (31). In general, restriction sites were chosen to facilitate modular swapping of parts via restriction enzyme cloning. A complete list of plasmids used in this study is provided in **Supplementary Data 1**. Plasmid maps are included as GenBank files in **Supplementary Data 2**.

Plasmid preparation

TOP10 *E. coli* were grown overnight in 100 mL LB with the appropriate selective antibiotic. The following morning, cells were pelleted at 3,000×g for 10 min and then resuspended in 4 mL of a solution of 25 mM Tris pH 8.0, 10 mM EDTA, 15% sucrose, and 5 mg/mL lysozyme (Fisher Scientific #AAJ6070114). Cells were lysed for 15 min by addition of 8 mL of a solution of 0.2 M NaOH and 1% SDS, followed by neutralization with 5 mL 3 M sodium acetate (pH 5.2). The precipitate was pelleted by centrifugation at 9,000×g for 20 min. Supernatant was decanted and treated with RNase A for 1 h at 37°C. 5 mL phenol chloroform was added, and the solution was mixed and then centrifuged at 7,500×g for 20 min. The aqueous layer was removed and subjected to another round of phenol chloroform extraction with 7 mL phenol chloroform (Fisher Scientific #BP1752I). The aqueous layer was then decanted and subjected to an isopropanol precipitation (41% final volume isopropanol, 10 min at room temperature—approximately 22°C, 9,000×g for 20 min), and the pellet was briefly dried and resuspended in 420 µL water. The DNA mixture was incubated on ice for at least 12 h in a solution of 6.5% PEG 20,000 and 0.4 M NaCl (1 mL final volume). DNA was precipitated by centrifugation at 21,000×g for 20 min. The pellet was washed once with ethanol, dried for several h at 37°C, and resuspended for several h in TE buffer (10 mM Tris, 1 mM EDTA, pH 8.0). DNA purity and concentration were confirmed using a Nanodrop 2000 (Thermo Fisher).

Cell culture

The HEK293FT cell line was purchased from Thermo Fisher/Life Technologies (RRID: CVCL_6911 [https://web.expasy.org/cellosaurus/CVCL_6911]) and was not further authenticated. Cells were cultured in DMEM (Gibco #31600-091) with 4.5 g/L glucose (1 g/L, Gibco #31600-091; 3.5 g/L additional, Sigma #G7021), 3.7 g/L sodium bicarbonate (Fisher Scientific #S233), 10% FBS (Gibco #16140-071), 6 mM L-glutamine (2 mM, Gibco #31600-091; 4 mM additional, Gibco #25030-081), penicillin (100 U/µL), and streptomycin (100 µg/mL) (Gibco #15140122), in a 37°C incubator with 5% CO_2. Cells were subcultured at a 1:5 to 1:10 ratio every 2–3 d using Trypsin-EDTA (Gibco #25300-054). The HEK293FT cell line tested negative for mycoplasma with the MycoAlert Mycoplasma Detection Kit (Lonza #LT07-318).

Transfection

Transient transfection of HEK293FT cells was conducted using the calcium phosphate method. Cells were plated at a minimum density of 1.5×10^5 cells per well in a 24-well plate in 0.5 mL DMEM, supplemented as described above. For surface staining experiments, cells were plated at a minimum density of 3.0×10^5 cells per well in a 12-well plate in 1 mL supplemented DMEM. For microscopy experiments, glass coverslips placed in 6-well plates were coated in a 0.1 mg/mL solution of poly-L-lysine hydrobromide (Sigma #P6282) for 5 min and left to dry overnight before plating 6×10^5 cells per well in 2 mL DMEM. After at least 6 h, by which time the cells had adhered to the plate, the cells were transfected. For transfection, plasmids were mixed in H_2O, and 2 M $CaCl_2$ was added to a final concentration of 0.3 M $CaCl_2$. The exact DNA amounts added to the mix per well and plasmid details for each experiment are listed in **Supplementary Data 3**. This mixture was added dropwise to an equal-volume solution of 2× HEPES-Buffered Saline (280 mM NaCl, 0.5 M HEPES, 1.5 mM Na_2HPO_4) and gently pipetted up and down four times. After 2.5–4 min, the solution was mixed vigorously by pipetting ten times. 100 µL of this mixture was added dropwise to the plated cells in 24-well plates, 200 µL was added to the plated cells in 12-well plates, or 400 µL was added to the plated cells in 6-well plates, and the plates were gently swirled. The next morning, the medium was aspirated and replaced with fresh medium. In some assays, fresh medium contained ligand and/or vehicle as described in **Supplementary Table 1** and indicated in figure legends.

Typically at 36–48 h post-transfection and at least 24 h post-media change, cells were harvested. As noted in figure captions, some experiments involved treatment with ligand or vehicle at later time points. In these cases, medium was still replaced the morning after transfection, and ligand diluted in serum-free DMEM was added as indicated. Cells were harvested for flow cytometry using FACS Buffer (FB; PBS pH 7.4, 2–5 mM EDTA, 0.1% BSA) or using 0.05% Trypsin-EDTA (Thermo Fisher Scientific #25300120) for 5 min followed by quenching with medium. The resulting cell solution was added to at least 2 volumes of FB. Cells were spun at 150×g for 5 min, FB was decanted, and fresh FB was added. All experiments were performed in biologic triplicate.

Luciferase assays

Some functional assays used a luciferase readout (Dual-Glo, Promega #E2940) measured by a microplate reader (BioTek Synergy H1). Cells were transfected in biological triplicate with MESA receptor chains, an inducible Firefly luciferase, a constitutive *Renilla* luciferase, an inducible EYFP, a constitutive EBFP2, and an empty vector (as needed to maintain equal total plasmid mass across conditions). The day after transfection, vehicle and ligand treatments were applied during the medium change. Two days after transfection, EBFP2 and EYFP served as confirmatory microscopy readouts, and the two luciferase signals were quantified. Dual-Glo kit reagents were stored and prepared per the manufacturer-supplied instructions and equilibrated to room temperature; all steps were carried out at room temperature. At the time of assaying, medium was aspirated from cell cultures and cells were washed with PBS. Passive lysis buffer stock (5X, Promega #E1941) was diluted in water, and the diluted buffer (120 µL, 1X) was added to each well. Plates were placed on a rocker for 15 min, after which the lysates were transferred into a 1.5 mL Eppendorf tube. Each tube was vortexed (15 s), and tubes were centrifuged (15,000×g, 30 s). 30 µL of supernatant was pipetted from each tube into a well of a 96-well plate (Thermo Fisher Scientific #655906). Luciferase reagent (30 µL, a volume equal to that of cell lysate) was pipetted into each well and mixed. Plates were incubated by rocking in the dark for 15 min.

Data were collected using the microplate reader's luminescence fiber. For Firefly luciferase signal acquisition, autogain was set to scale the brightest wells to a value of 5,000,000 RLU. Integration time was

set to 1 s and three technical replicate measurements per well were obtained. Stop & Glo reagent (30 µL, equal to that of the previous reagent) was added to each well, and plates were incubated by rocking in the dark for 15 min. For *Renilla* luciferase signal, the gain was set to 200, the integration time was set to 5 s, and three technical replicate measurements per well were obtained. For each well, the mean of the three technical replicates was calculated for each of the two luciferase readouts. Subsequently, the autoluminescence signal (calculated from the mean of the three vector-only transfected wells) was subtracted from each condition to background-normalize for each of the two luciferase readouts, respectively. Then for each biological replicate, Firefly luciferase signal was divided by *Renilla* luciferase signal. Quotients were linearly scaled such that the mean of the quotients for a condition transfected with reporter only was equal to 1 a.u. Error was propagated accordingly.

Western blotting

For Western blotting, HEK293FT cells were plated at 7.5×10^5 cells per well in 2 mL DMEM in 6-well plates and transfected as above, using 400 µL transfection reagent per well (the reaction scales with the volume of medium). At 36–48 h after transfection, cells were lysed with 500 µL RIPA (150 mM NaCl, 50 mM Tris-HCl pH 8.0, 1% Triton X-100, 0.5% sodium deoxycholate, 0.1% sodium dodecyl sulfate) with protease inhibitor cocktail (Pierce/Thermo Fisher #A32953) and incubated on ice for 30 min. Lysate was cleared by centrifugation at 14,000×g for 20 min at 4°C, and supernatant was harvested. A BCA assay was performed to determine protein concentration, and after a 10 min incubation in Lamelli buffer (final concentration 60 mM Tris-HCl pH 6.8, 10% glycerol, 2% sodium dodecyl sulfate, 100 mM dithiothreitol, and 0.01% bromophenol blue) at 70°C (or 100°C for experiments that involved multiple co-transfected MESA receptors), protein (0.5 µg for experiments that were imaged with film, 10 to 25 µg for experiments that were imaged digitally) was loaded onto a 4–15% Mini-PROTEAN TGX Precast Protein Gel (Bio-Rad) and run either at 50 V for 10 min followed by 100 V for at least 1 h, or at 100 V for at least 1 h. Wet transfer was performed onto an Immuno-Blot PVDF membrane (Bio-Rad) for 45 min at 100 V. Ponceau-S staining was used to confirm protein transfer. Membranes were blocked for 30 min with 3% milk in Tris-buffered saline pH 8.0 (TBS pH 8.0: 50 mM Tris, 138 mM NaCl, 2.7 mM KCl, HCl to pH 8.0), washed once with TBS pH 8.0 for 5 min, and incubated for 1 h at room temperature or overnight at 4°C in primary antibody (Mouse-

anti-FLAG M2 [Sigma #F1804, RRID: AB_262044 [http://antibodyregistry.org/AB_262044]), diluted 1:1000 in 3% milk in TBS pH 8.0. Primary antibody solution was decanted, and the membrane was washed once with TBS pH 8.0 and then twice with TBS pH 8.0 with 0.05% Tween, for 5 min each. Secondary antibody (HRP-anti-Mouse [CST 7076, RRID: AB_330924 [http://antibodyregistry.org/AB_330924]), diluted 1:3000 in 5% milk in TBST pH 7.6 (TBST pH 7.6: 50 mM Tris, 150 mM NaCl, HCl to pH 7.6, 0.1% Tween), was applied for 1 h at room temperature, and the membrane was washed three times for 5 min each time with TBST pH 7.6. The membrane was incubated with Clarity Western ECL Substrate (Bio-Rad) for 5 min, and then either exposed to film, which was developed and scanned, or digitally captured using an Azure c280 (Azure Biosystems). Images were cropped with Photoshop CC (Adobe). No other image processing was employed. Original images will be provided in **Source Data 2 upon final submission in a digital repository**.

Expression normalization of MESA chains

Scanned Western blot images were imported into ImageJ and analyzed using the analyze gel feature. The intensity for each MESA chain band was quantified and reported as the percent of the total signal from all MESA bands on the blot; the same calculation was performed for all of the NanoLuciferase bands. This analysis was repeated for multiple images captured for each blot (including a range of exposure times to minimize bias) with non-detectable and saturated bands excluded from the analysis. The calculated intensity was averaged across all exposure times, and then MESA intensity (expression level) was divided by the NanoLuciferase intensity (expression level). This value was compared to the intensity calculated for the CD28-TMD rapamycin-binding TC sample, which was included on each blot as an internal cross-comparison control. This calculated ratio was used to adjust the doses of plasmids used for transfections in subsequent rounds of experiments, which were again evaluated by Western blots. The set of plasmid doses used in each round is in **Supplementary Table 6**.

Immunohistochemistry

For surface staining, HEK293FT cells were plated at 3×10^5 cells per well in 1 mL DMEM in 12-well plates and transfected as described above, using 200 μL transfection reagent per well. At 36–48 h after

transfection, cells were harvested with 500 μL FB and spun at 150×g at 4°C for 5 min. For the experiment in **Supplementary Fig. 14** in which multiple harvest methods were compared, some samples were harvested using 0.05% Trypsin-EDTA (3 min or 10 min incubation, 37°C), which were then quenched with medium and added to two volumes of FB. FB was decanted, and 50 μL fresh FB and 10 μL human IgG (Human IgG Isotype Control, ThermoFisher Scientific #02-7102, RRID: AB_2532958, stock concentration 1 mg/mL) was added. Cells were incubated in this mixture at 4°C for 5 min. 5 μL FLAG tag antibody (Anti-DDDDK-PE, Abcam ab72469, RRID: AB_1268475, or Anti-DDDDK-APC, Abcam ab72569, RRID: AB_1310127) was added at a concentration of 0.5 μg per sample and cells incubated at 4°C for 30 min. Following incubation, 1 mL FB was added, cells were spun at 150×g at 4°C for 5 min, and supernatant was decanted. This wash step was repeated two more times to total three washes. After decanting supernatant in the final wash, 1–3 drops FB were added.

Analytical flow cytometry

Flow cytometry was run on a BD LSR Fortessa Special Order Research Product (Robert H. Lurie Cancer Center Flow Cytometry Core). Lasers and filter sets used for data acquisition are listed in **Supplementary Table 2** (for experiments involving reporter expression), **Supplementary Table 3** (for experiments quantifying receptor expression on the cell surface), and **Supplementary Table 4** (for experiments involving FRET). Approximately 2,000–3,000 single transfected cells were analyzed per sample, using a single transfection control or, when available, multiple transfected fluorophores for gating (e.g., mCerulean+/mVenus+ cells were classified as the subset of transfected cells of interest for FRET experiments).

Samples were analyzed using FlowJo v10 software (FlowJo, LLC). Fluorescence data were compensated for spectral bleed-through. Additionally, spectral bleed-through compensation in FRET experiments included compensation of the fluorescence of either mCerulean or mVenus out of the AmCyan channel. As shown in **Supplementary Fig. 1**, the HEK293FT cell population was identified by FSC-A vs. SSC-A gating, and singlets were identified by FSC-A vs. FSC-H gating. To distinguish transfected from non-transfected cells, a control sample of cells was generated by transfecting cells with a mass of pcDNA (empty vector)

equivalent to the mass of DNA used in other samples in the experiment. For the single-cell subpopulation of the pcDNA-only sample, a gate was made to identify cells that were positive for the constitutive fluorescent protein used as a transfection control in other samples, such that the gate included no more than 1% of the non-fluorescent cells.

Quantification of reporter output

The mean fluorescence intensity (MFI) for each relevant channel of the single-cell transfected population was calculated and exported for further analysis. To calculate reporter expression, MFI in the FITC or PE-Texas Red channel (depending on the experiment) was averaged across three biologic replicates. From this number, cell autofluorescence was subtracted. To calculate cell autofluorescence, in each experiment, a control group of cells transfected with DNA encoding the fluorescent protein transfection control and pcDNA was used. The background-subtracted MFI was converted to Molecules of Equivalent Fluorescein (MEFLs) or Molecules of Equivalent PE-Texas Red (MEPTRs); as shown in **Supplementary Fig. 2**, to determine conversion factors for MFI to MEFLs and for MFI to MEPTRs, Rainbow Calibration Particles (Spherotech #RCP-30-5) or UltraRainbow Calibration Particles (Spherotech #URCP-100-2H) were run with each flow cytometry experiment. These reagents contain six (RCP) or nine (URCP) subpopulations of beads, each with a known number of various fluorophores. The total bead population was identified by FSC-A vs. SSC-A gating, and bead subpopulations were identified through two fluorescent channels. MEFL and MEPTR values corresponding to each subpopulation were supplied by the manufacturer. A calibration curve was generated for the experimentally determined MFI vs. the manufacturer-supplied MEFLs or MEPTRs, and a linear regression was performed with the constraint that 0 MFI equals 0 MEFLs or MEPTRs. The slope from the regression was used as the conversion factor, and error was propagated. Fold differences were calculated by dividing reporter expression with ligand treatment by the reporter expression without ligand treatment (vehicle). Standard error was propagated through all calculations.

Quantification of FRET by flow cytometry

The mCerulean+/mVenus+ population was distinguished from samples transfected with the transfection control and pcDNA only, mCerulean only, and mVenus only. This gate was drawn such that less than 1%

of the listed single-color samples were included. The normalized FRET (NFRET) parameter (32) was defined in the FlowJo workspace by dividing the compensated fluorescence intensity (FI) of a cell in the AmCyan channel by the square root of the product of the compensated FI of that cell in the Pacific Blue and FITC channels, as described by equation (1):

$$NFRET = \frac{Comp\ AmCyan\ FI}{\sqrt{Comp\ Pacific\ Blue\ FI \times Comp\ FITC\ FI}} \quad (1)$$

Average NFRET metrics were calculated for controls included in each experiment, including a negative control (cytosolic mCerulean and mVenus co-transfected) and positive control (membrane-tethered mCerulean-mVenus fusion protein). A calibrated NFRET parameter was defined based on the negative and positive FRET controls such that the NFRET of all samples is scaled linearly between these controls, as described by equation (2):

$$NFRET_{Calibrated} = \frac{(NFRET - NFRET_{negative\ control})}{(NFRET_{positive\ control} - NFRET_{negative\ control})} \quad (2)$$

The calibrated NFRET metrics were exported, along with each MFI in the relevant channels of the single-cell, transfected, mCerulean+/mVenus+ population for further analysis. In this study, all plotted NFRET metrics are calibrated values, and all FRET MFI are compensated. Fold differences were calculated by dividing NFRET in the presence of ligand by NFRET in the absence of ligand (presence of vehicle only). Standard error was propagated through all calculations.

Confocal microscopy

Confocal microscopy was performed on a Leica SP5 II laser scanning confocal microscope (Northwestern Chemistry of Life Processes Institute, Biological Imaging Facility) with a 100× (1.44 NA) oil-immersion objective. Coverslips were removed from media and mounted on a glass slide immediately before imaging. Ten fields of view were captured for each sample. Fields of view were selected using the brightfield channel to identify areas with adherent cells, and the z-axis was adjusted to focus on the central plane of most cells within the field of view before exposing the cells to lasers. All images were captured at a 512×512 image resolution with a scanning speed of 400 Hz. Excitation and emission settings were selected depending on which fluorophore (donor (D) or acceptor (A)) was excited and which emission was captured. The excitation

and emission setup is described in **Supplementary Table 5**. HyD voltage settings were held constant for all samples within each experiment.

Quantification of FRET by image processing

Images were exported as stacks and separated into single-channel images using Fiji software. A custom image processing script was produced in MATLAB to import single-channel images into matrices (**Supplementary Software**). To describe channels throughout this section, DD indicates that the donor was excited and emission from the donor was captured, AA indicates that the acceptor was excited and emission from the acceptor was captured, and DA indicates that the donor was excited and emission from the acceptor was captured. Empty vector-only (pcDNA) transfected samples were used to identify the upper limit of autofluorescence in each channel (DD, AA, DA), and thresholds were defined as the 99.9th percentile of fluorescence of pixels in the vector-only samples in each channel. Pixels below this threshold were set to an intensity of zero. Saturated pixels were also removed from the matrices. Next, respective donor-only and acceptor-only controls (single-receptor transfections) were used to calculate spectral bleed-through parameters. These parameters, as defined in equations (3–6), were calculated by averaging across all pixels in ten fields of view, excluding pixels with infinite or undefined values. Intensities (I) are subscripted with DD, AA, or DA to indicate the excitation and emission conditions, and with (D) or (A) to indicate that this parameter was calculated using donor-only or acceptor-only samples, respectively.

$$a = \frac{I_{DA(A)}}{I_{AA(A)}} \quad (3) \qquad b = \frac{I_{DD(A)}}{I_{AA(A)}} \quad (4)$$

$$c = \frac{I_{AA(D)}}{I_{DD(D)}} \quad (5) \qquad d = \frac{I_{DA(D)}}{I_{DD(D)}} \quad (6)$$

The parameters calculated for each pair of receptors were used to subtract the contribution of donor and acceptor fluorescence from the FRET channel fluorescence on a pixel-by-pixel basis as described in equation (7) and as reported previously (33). This step produced a corrected FRET fluorescence intensity (F_c):

$$F_c = I_{DA} - a(I_{AA} - cI_{DD}) - d(I_{DD} - bI_{AA}) \quad (7)$$

NFRET is calculated by normalizing F_c to the square root of the product of the donor and acceptor fluorescence intensities on a pixel-by-pixel basis as described in equation (8) and as reported previously (32).

$$NFRET = \frac{F_c}{\sqrt{I_{AA} \times I_{DD}}} \quad (8)$$

NFRET values were exported across pixels within each field of view and across all fields of view, then averaged to generate a mean NFRET metric for the entire sample. Corrected FRET intensity and NFRET matrices were plotted and visualized as processed images.

Ectodomain distance estimations

Published crystal structures for ligand-bound ectodomains (ECDs) were analyzed using Chimera (FKBP/FRB PDB: 3FAP (34), GID1/DELLA PDB: 2ZSH (35), ABI1/PYL1 PDB: 3KDJ (36), G6-311 VEGF scFv PDB: 2FJG (37), B20-4.1 VEGF scFv PDB: 2FJH (37)). Residues that correspond to the C-termini used in our experimental receptor system were identified, and inter-termini distances were measured.

Statistical analyses

Unless otherwise stated, three independent biologic replicates were evaluated for each condition. The data shown reflect the mean across these biologic replicates of the MFI of approximately 2,000–3,000 single, transfected cells or the mean NFRET or NFRET fold difference of approximately 2,000–3,000 single, transfected, mCerulean+/mVenus+ cells. Error bars represent the standard error of the mean (S.E.M.).

ANOVA tests and Tukey's HSD tests were performed using RStudio. Tukey's HSD tests were performed with $\alpha = 0.05$. Pairwise comparisons were made using a two-tailed Welch's *t*-test, which is a version of Student's *t*-test in which the variance between samples is treated as not necessarily equal. Two-tailed Welch's *t*-tests were performed in GraphPad. To decrease the false discovery rate, the Benjamini-Hochberg (BH) procedure was applied to each set of tests per figure panel; in all tests, after the BH procedure, the null hypothesis was rejected for *p*-values < 0.05. The outcomes for each statistical test are provided in the figure captions, and additional details for some panels are in referenced supplementary notes. **Supplementary Note 1** includes the outcomes for two-way ANOVA tests followed by Tukey's HSD test for

Fig. 4a,b and **Fig. 5a–f**. **Supplementary Note 2** include the outcomes for three-way ANOVA tests followed by Tukey's HSD test for **Fig. 4c**, **Supplementary Fig. 11**, **Fig. 5a–f**, and **Supplementary Fig. 28b**. **Supplementary Note 3** includes the outcomes for two-tailed Welch's *t*-tests followed by BH procedure for **Supplementary Fig. 13b**.

RESULTS

Protease tuning to reduce background

We initially focused on the goal of decreasing MESA receptor background signaling by investigating two strategies that we hypothesized could modulate the kinetics of proteolytic *trans*-cleavage. In our initial development of MESA (25), we used prior biochemical analyses of the TEV protease (TEVp) (38-41) to vary cleavage kinetics by mutating the P1' site of the protease recognition sequence (PRS: ENLYFQX) on the target chain (TC). This enabled identification of a kinetic regime in which dimerization-inducible signaling was feasible. To investigate whether this tuning could be extended to reduce background, we first explored a strategy in which PRS mutations were combined with modifications to the protease chain (PC) that are reported to diminish TEVp cleavage kinetics (38-41)—mutation of residues 217 and 219 of TEVp and inclusion of the native autoinhibitory peptide (AIP: ELVYSQ) on the TEVp C-terminus. In a functional assay, each new TC-PC combination did produce lower background compared to the base case, however the ligand-induced fold difference (F.D.) in reporter expression did not increase, so we chose not to pursue these variants (**Supplementary Fig. 3a–c**).

We next explored a second strategy that is motivated by crystallographic evidence that the AIP can reside in the TEVp active site (41) and by an observation that the PRS and AIP are similar in sequence (**Supplementary Fig. 3d**). We hypothesized that by placing variants of the PRS or AIP on the TEVp C-terminus, these peptides might reversibly occupy the TEVp active site such that TC-PC *trans*-cleavage is inhibited during transient diffusive encounters but cleavage eventually occurs in the context of sustained ligand binding-induced chain dimerization (**Fig. 1b**). In studying these motifs, and in subsequent experiments, we replaced rapamycin as the ligand with a rapamycin analog (rapalog), which we found to

produce generally higher ligand-induced reporter expression compared to rapamycin (**Supplementary Fig. 4**). Of the ten motifs examined, all decreased both background and ligand-induced signaling. For four of the motifs (ELVYSQ, ELVYSQM, ELVYSQA, ELVYSQK), F.D. increased slightly compared to the base case. Therefore, adding active site-occupying peptides can reduce background and tune some aspects of receptor performance, but on its own, this effect is modest.

Stabilizing PC expression

In prior work, we observed that PC surface expression is often lower than TC surface expression (25, 29), and we hypothesized that some aspects of PC design might render this chain less stable. Western blot analysis showed expression of the full-length PC as well as a smaller fragment, the size of which was consistent with juxtamembrane cleavage; as this pattern was observed even when TEVp was mutated to be catalytically inactive, we attribute the cleavage to endogenous protease activity (**Supplementary Fig. 5a–c**). PC instability is potentially problematic because the residual membrane-tethered ectodomain (ECD) could function as a competitive inhibitor of intact receptors, and the TEVp released into the cytosol could contribute to background signaling. To explore alterations that might prevent spontaneous PC cleavage, we first varied the sequence of the PC inner linker (PCIL) that connects the TEVp and transmembrane domain (TMD) by introducing positively charged residues and sequences from native receptors. These substitutions seemed to improve protein stability, reducing the appearance of the originally observed juxtamembrane cleavage product (**Supplementary Fig. 5d**). However, these substitutions also diminished functional performance, by increasing background signaling and therefore decreasing ligand-induced F.D.; this effect could not be overcome by decreasing the PC plasmid dose, to compensate for the increased levels of intact PC, without diminishing ligand-induced signaling (**Supplementary Fig. 5e,f**). These substitutions also reduced surface expression of the PC (**Supplementary Fig. 5g**). Although it is not clear why each substitution conferred these undesirable effects, it was clear that PCIL substitution alone did not address PC stability or background signaling via a useful mechanism, and so we turned to other modifications as alternative approaches.

Varying the transmembrane domain

All previous MESA receptor designs (25, 29) employ a form of the CD28 TMD which is commonly used in chimeric antigen receptors (CARs); this TMD differs somewhat from the native CD28 TMD sequence. We hypothesized that varying the TMD could confer desirable effects on receptor performance based upon several insights from natural receptor biology. For example, while the CD28 receptor clusters as a member of the immunological synapse formed between a T cell and an antigen-presenting cell (42, 43), receptor tyrosine kinases (RTKs) signal by a variety of mechanisms including ligand-induced dimerization, ligand-induced rotation, and clustering, and the TMD plays a critical role in these mechanisms (44). Moreover, different RTK TMDs dimerize with varying propensities (45), providing a potential handle for receptor tuning. In other engineered receptors such as CARs, TMD choice has proven to be a useful handle for tuning interactions between receptor chains and modulating the strength of ligand binding-induced receptor signaling (46, 47). We selected a panel of seven native RTK TMDs with a range of dimerization propensities, in addition to two synthetic TMDs (48) and substituted these for the CD28-TMD (**Fig. 2a**). TMD substitution had a substantial effect on receptor expression, and in some cases this effect differed for the TC and PC (**Supplementary Fig. 6a**). To evaluate the effects of TMD substitution in a manner that is independent of the effects on expression level, we normalized protein expression (**Fig. 2b)** by varying plasmid doses through iterative Western blot analyses **(Supplementary Fig. 6a–f**). We observed that all of the TMD substitutions except for FGFR1-TMD resolved the PC cleavage issue observed with CD28-TMD (**Fig. 2b, Supplementary Figure 5)**, and all substitutions altered surface expression (**Supplementary Figure 7**). In functional evaluations using TC:PC protein expression ratios of approximately 1:1, TMD substitution conferred substantial effects on performance **(Fig. 2c**)**.** Notably, employing the TMDs from GpA, FGFR1, and FGFR4 increased the ligand-induced signaling compared to the CD28-TMD, leading to high-performing systems. Conversely, utilizing the TMDs from FGFR2, FGFR3, EphA4, and VEGFR1 did not result in receptors that were capable of signaling.

To determine whether using different TMDs on the TC and PC could yield further improvements, we evaluated the 100 (10×10) pairwise TC-PC combinations. In our initial screen, most TCs that conferred little or no detectable ligand-induced signaling when paired with a PC bearing the same TMD (matched pairs) also showed little or no ligand-induced signaling when paired with a different TMD PC (mixed pairs)

(**Supplementary Fig. 8a,b**). An exception to this trend is the VEGFR1-TMD, which showed some ligand-induced signaling when paired with a PC containing the CD28, GpA, FGFR1, FGFR3, FGFR4, or Valine TMD resulting in improved F.D. (**Supplementary Fig. 8a,b**). Notably, many other mixed TMD pairs also showed substantially improved performance compared to the matched CD28-TMD base case, leading to F.D. as high as 97 (**Fig. 2d**). Together, these results suggest that TMD choice is a key determinant of receptor performance and a rich target for tuning.

Investigating the role of the TMDs

Given the promising results obtained with certain TMD choices, we next sought mechanistic insight into the roles of these domains in MESA signaling. For native receptors, TMDs can affect both localization and function (44), but how this choice affects synthetic receptor function is unexplored. Since some TMD sequence motifs mediate receptor homodimerization, we hypothesized that TMD choice might affect MESA receptor performance by modulating the propensity for chains to associate. We first evaluated TMD association computationally using TMDOCK, a tool that uses amino acid sequence to predict TMD association by simulating alpha helix packing arrangements and conducting local energy minimization (49) (**Supplementary Fig. 9a–c**). This analysis predicted differences in matched-TMD interactions, although the predicted trends only partially matched our experimental observations. For example, the FGFR1-TMD is predicted to exhibit a high propensity to homodimerize, which is consistent with the observed high background signal (**Fig. 2c**). However, the GpA-TMD is also predicted to homodimerize (with more stability than the CD28-TMD) but this was not evident from the background signal in functional assays. Thus, we sought to build further insight through experimental characterization of full-length proteins in cells. To this end, we adapted a Förster resonance energy transfer (FRET)-based assay (32, 50) to quantify MESA receptor association (**Fig. 3a**). We replaced the TC and PC intracellular domains (ICDs) with mVenus or mCerulean—fluorescent proteins that exhibit FRET in a manner dependent on spatial co-localization (FRET occurs within a Förster radius of 52.4 Å (51, 52)). Using this assay, ligand-dependent and ligand-independent association should each be quantifiable by measuring acceptor (mVenus) fluorescence upon donor (mCerulean) excitation. We chose to investigate three TMDs to help explain our preceding observations: CD28-TMD for its predicted large number of energetically favorable modes of association

(**Supplementary Fig. 9**), propensity to cluster (45), and use in previous MESA receptors (25, 29); GpA-TMD for its documented high propensity to homodimerize (45, 53); and FGFR4-TMD for its documented (45) and predicted low propensity to dimerize (**Supplementary Fig. 9**) and high performance in functional assays (**Fig. 2c**).

To establish a high-throughput workflow that yields single-cell resolution data, we first validated a reported approach (50) to quantify FRET by flow cytometry and normalized this metric to account for single-cell level variation in protein expression. Expression normalization is particularly useful, and perhaps necessary, for any scenario in which expression levels are heterogeneous between cells. In this approach, single-cell mCerulean donor fluorescence (λ_{ex} = 405nm, λ_{em} = 450/50nm), mVenus acceptor fluorescence (λ_{ex} = 488nm, λ_{em} 530/30nm), mVenus FRET fluorescence (λ_{ex} = 405nm, λ_{em} 530/30nm), and mIRFP670 fluorescence (λ_{ex} = 640nm, λ_{em} 670/30nm) are quantified by flow cytometry. Single-color samples are analyzed to apply post-hoc linear compensation for spectral bleed-through across fluorophore and FRET channels using an expression range that encompasses the receptor samples (**Fig. 3b**, **Supplementary Fig. 10a**), and then samples with transfected cells (mIRFP670+) that are both mCerulean+ and mVenus+ are analyzed (**Supplementary Fig. 1a**, **Supplementary Fig. 10b**).

To quantify FRET efficiency, we evaluated two possible metrics using a model system: cells expressing either a positive control (an mVenus-mCerulean fusion protein that is expected to exhibit strong FRET (54)) or a negative control (mVenus and mCerulean expressed as separate proteins that are expected not to exhibit FRET). The first metric, FRET MFI, was quantified using unprocessed fluorescence intensity in the FRET channel. This metric correlated linearly with donor fluorescence and acceptor fluorescence, and it was higher for the fusion protein than for the non-fused control (**Fig. 3c**). For the second metric, normalized FRET (NFRET), (32, 55) the FRET signal in each cell was normalized to that cell's donor and acceptor fluorophore expression levels (**Fig. 3d**). Unlike FRET MFI, NFRET had a low correlation with fluorophore expression level, confirming the intended normalization and enabling analysis across two orders of magnitude in donor and acceptor fluorescence (**Fig. 3d, Supplementary Fig. 10c**). Although each of these metrics can report *whether* FRET occurs in this model system, NFRET provides better quantitative

resolution separating the two control populations (**Fig. 3e**), and since it inherently controls for variation in protein expression, we utilized this metric exclusively going forward. As a final validation of our analytical pipeline, and to enable comparison of our methods with more typical microscopy-based FRET analyses, we adopted our method to a confocal microcytometry workflow (**Methods**), which confirmed the patterns observed by flow cytometry (**Supplementary Fig. 11**).

Having validated this FRET assay, we next employed it to interrogate the contribution of TMD choice to MESA chain interactions. Across the three TMD choices examined, NFRET increased significantly upon ligand treatment, F.D. values were similar (**Fig. 4a**), and ligand dose responses were similar (**Fig. 4b, Supplementary Fig. 12**). We next examined mixed TMD choices and again observed that constructs showed similar and significant ligand-inducible NFRET (**Fig. 4c**). This pattern held upon swapping the fluorophore domains (**Supplementary Fig. 13**), testing different cell harvest methods (**Supplementary Fig. 14**), and measuring NFRET by confocal microscopy (**Supplementary Fig. 15**). To investigate whether TMD choice affects the dynamics of receptor signaling, we performed a time course analysis and observed that MESA receptors containing CD28-TMD and FGFR4-TMD exhibit similar kinetics of ligand-induced NFRET in both matched and mixed pairs (**Fig. 4d, Supplementary Fig. 16**). Moreover, the onset of FRET was observed within 15 min of ligand treatment in some cases, indicating that this signal is attributable to the ligand-induced association of existing chains, rather than potential ligand-induced stabilization of newly synthesized chains. Although ligand treatment modestly increased the accumulation of individual chains over a long interval (e.g., 27 h) (**Supplementary Fig. 17**), this modest increase would not be expected to substantially impact NFRET, particularly because this metric accounts for protein expression level (**Fig. 3d**). Finally, we evaluated whether MESA chains compete with one another for TMD-mediated interactions using a cold chain competition assay (**Fig. 4e**) employing a non-fluorescent mVenus mutant (**Supplementary Fig. 18a**). The introduction of a cold chain containing any TMD led to reduced NFRET between all matched-TMD test chain variants by ~20%, with a slightly but significantly greater decrease when CD28-TMD–containing test chains were disrupted by a CD28-TMD cold chain than by another cold chain (**Fig. 4e**, **Supplementary Fig. 18b**). This result is consistent with the slightly higher NFRET observed for CD28-TMD receptors (treated with vehicle only) when this case is compared to that of other TMD

choices (**Fig. 4a**). Together, these results indicate a slightly higher propensity for CD28-TMDs to self-associate compared to FGFR4-TMDs and GpA-TMDs in the MESA receptor context, which is insufficient to explain the differences observed across TMD choices in our functional assays. Thus, although TMD choice substantially affects MESA receptor performance, it does not appear to do so by modulating the general propensity for chains to associate in the absence or presence of ligand.

Given these observations, we hypothesized that TMD choice may impact receptor dimerization geometry in a manner that affects *trans*-cleavage efficiency but does not affect overall chain association. To test this hypothesis, we utilized a panel of synthetic TMDs that were designed to dimerize in a specific fashion that systematically varies the orientation of dimerization across the panel (**Fig. 4f**); these TMDs were previously used to study geometric constraints on juxtamembrane regions of RTKs (56). TMDOCK analysis predicted that the panel of TMDs can dimerize in configurations with distances between TMD C-termini (at the inner leaflet of the membrane) ranging from 5.4–16.0 Å (**Supplementary Fig. 19**). Although this analysis does not account for any geometric constraints that might be imposed by other domains of the MESA chains, we hypothesized that if TMD interaction geometry does indeed impact *trans*-cleavage efficiency, then MESA receptors built using this panel of synthetic TMDs would exhibit differential signaling in a functional assay. In support of this hypothesis, ligand-induced signaling indeed varied across the panel and decreased substantially as the residues mediating dimerization were moved away from the inner leaflet of the membrane (**Fig. 4g**). This effect could not be explained either by differences in expression level of the receptors—the chains with the lowest magnitude of ligand-induced signaling were the most highly expressed (**Supplementary Fig. 20a**)—or by differences in ligand-induced MESA protein accumulation, which was modest and similar across the panel (**Supplementary Fig. 20b**), similar to the effect observed with FRET constructs (**Supplementary Fig. 17**). These data support the argument that TMD choice can alter the geometry in which receptor chains dimerize and that this can substantially impact the efficiency of MESA receptor *trans*-cleavage.

Extending design rules to new synthetic receptors

Given our new understanding of the role of TMD choice, we next investigated whether the observed trends would extend to MESA systems with different ECDs and ligands. To test this hypothesis, we first built two new MESA receptors to sense small molecules—gibberellin (GA3-AM is a cell-permeable analogue) and abscisic acid (ABA) (**Supplementary Fig. 21–26**)—and a third new MESA receptor to sense GFP (here we use co-expressed secreted GFP, sGFP, as an expedient testing system), and explored design considerations that are typically expected to be ECD-specific, such as how linker length affects expression and cell-surface localization (57, 58). Interestingly, functional assays revealed TMD-associated trends that were largely consistent across ECDs (**Fig. 5a–d**, **Supplementary Fig. 22**, **Supplementary Fig. 24**, **Supplementary Fig. 27**, **Supplementary Fig. 28**). The TMD choice for each chain significantly affected background signaling and induced signaling, and the interaction between TMD choices was also significant, indicating that the choice of TC TMD or PC TMD alone does not fully explain the trends (**Supplementary Note 2**). Additionally, the TMD choices together account for most of the variance in background and induced signaling observed (**Supplementary Note 1**). These observations indicate that satisfying any one design objective (e.g., maximize F.D., minimize background, etc.) requires choosing a pair of TMDs suited to that design goal. Additionally, some general trends held across the rapamycin MESA receptors and these three new receptors. For example, high background and modest induced signaling were observed for pairs including FGFR1-TMD TC, resulting in generally low F.D. Conversely, FGFR4-TMD–containing pairs often exhibited low background signaling and high F.D. (**Fig. 5a–d**). Overall, we conclude that some effects of TMD choice extend across multiple MESA receptors, and perhaps of equal utility, a limited scan of these TMD choices enables one to generate multiple new high-performing receptors.

We next investigated whether the observed effects of TMD choice might extend to synthetic receptors that operate by a distinct mechanism. To test this, we employed a recently reported MESA system in which ligand binding induces reconstitution of a mutant split TEVp. The reconstituted protease then acts upon a sequestered TF, enabling the TF to enter the nucleus and drive reporter expression (26) (**Fig. 5e**). We replaced the CD28-TMD used in the reported rapamycin-sensing base case (26) with other TMDs and also built GFP-sensing variants of these receptors. In functional assays, we again found that the TMD proved to be a useful handle for tuning performance (**Fig. 5e,f, Supplementary Fig. 29, Supplementary Fig. 30**). Background and ligand-induced signaling were again significantly affected by TMD choice for each chain

and the interaction between the TMD choices (**Supplementary Note 2**). Strikingly, across all mixed and matched TMD pairs, the ligand-induced signal was relatively consistent, which differs from the trends observed for the *trans*-cleavage mechanism. Moreover, for these receptors, using the CD28-TMD on only one chain resulted in very low background signaling, but using the CD28-TMD on both chains (as previously reported (26)) resulted in the highest background of all combinations tested. Statistical analysis showed that in this mechanism, the interaction between TMD choices accounts for most of the variance in background signaling observed (**Supplementary Note 1**). When considered together with the TMD competition experiment (**Fig. 4f**), these results suggest that the CD28-TMD has a propensity to aggregate in the absence of ligand; this effect can be problematic if both chains include this TMD, yet this same property can be useful if only one chain bears this TMD. Comparing these two distinct MESA receptor mechanisms suggests that whereas subtle geometric effects conferred by specific TMD pairs have a substantial impact on MESA receptors employing the original *trans*-cleavage mechanism, these nuances may have less impact upon the performance of receptors employing a distinct mechanism (26). Moreover, for both MESA receptor mechanisms examined, our initial model system generated insights enabling the design of novel receptors.

Finally, given these new insights into the important connection between MESA receptor geometry and functional performance, we sought to utilize these tools to guide the selection of new ligands and ligand-binding domains. We noted that for MESA receptors engineered to sense rapamycin, gibberellin, abscisic acid, or in previous work, vascular endothelial growth factor (VEGF) (5), there exist crystal structures enabling us to estimate the displacement between the C-termini of the ECDs when they are dimerized in the ligand-bound state (34-37). To determine whether this spatial variation is sufficient to impact intracellular receptor geometry, we again employed FRET analysis (employing the well-behaved FGFR4-TMD) to best decouple our investigation of this question from the effects of receptor geometry on *trans*-cleavage (**Fig. 6a, Supplementary Fig. 31**). Interestingly, ligand-induced NFRET fold difference showed a strong negative correlation with the ECD C-terminal distance, suggesting that one can predict some aspects of receptor structure and function from prior knowledge of the ECDs alone—an attractive feature for a modular design strategy. We confirmed that these effects were indeed attributable to receptor complex formation by

performing a combinatorial ligand-ECD orthogonality analysis (**Fig. 6b**). Notably, the VEGF-binding ECDs—which correspond to the largest ECD C-terminal distances evaluated—showed a *diminishment* in NFRET upon ligand treatment in both experiments, suggesting that ligand-induced dimerization might diminish, on average, transient inter-chain ICD interactions compared to the ligand-free state. These observations could help to explain why MESA receptors with shorter ECD C-terminal distances (e.g., for rapamycin-sensing) generally exhibit strong signaling, and they suggest that functional sensing of gibberellin, abscisic acid, and VEGF could be attributable to *trans*-cleavage that occurs over longer timescales than are required to confer FRET. Altogether, the analyses presented in this study provide powerful new insights into the connection between tunable protein design choices, biophysical consequences, and impacts on the performance of synthetic receptors (**Fig. 6c**).

DISCUSSION

A key finding of this study is that systematic re-evaluation of the MESA synthetic receptor system enabled identification of design modifications that substantially improve receptor performance. While some modifications had modest effects, TMD substitution proved to be a particularly useful handle for receptor tuning and optimization (**Fig. 2**). Some TMD combinations greatly decreased background signaling while maintaining or increasing ligand-induced signaling, yielding high-performing receptors with F.D. on the order of 100; by this metric, these rank among the best synthetic receptors reported to date (12, 18, 23). Moreover, evaluating a relatively small library of TMD variants enabled us to generate high-performing MESA receptors for three new ligands (**Fig. 5**). It is notable that even for the fully synthetic mechanism employed by MESA receptors, it was not clear ahead of time which design modification strategies would be most fruitful. These improvements were achieved largely by investigating MESA receptor biophysics using the approaches and strategies typically employed to study natural receptors. There likely exists substantial room for improving synthetic receptor systems—a recent report evidences the utility of applying this approach to improve synNotch (24)—and powerful tools developed by the receptor biophysics community comprise substantial yet underutilized potential.

An integral part of this investigation was the use of flow cytometric FRET; this technique enabled us to link disparate observations and build understanding. FRET has generally proven useful for elucidating native receptor mechanisms, and these experiments typically employ confocal microscopy (59-61). We employed a substantially more high-throughput assay that provides single-cell resolution—thousands of individual cells per sample—by adapting a reported flow cytometry workflow (50) to this investigation. A key utility of the NFRET metric is that it enables comparisons across a heterogeneous population of cells by expression-normalizing FRET. To our knowledge, this is the first application of flow-FRET to characterize synthetic receptors, and this approach may be useful for studying and optimizing systems beyond MESA.

Altogether, this investigation provides new mechanistic insights into how TMD choice impacts MESA receptor performance. Only the CD28-TMD used in previous MESA receptors (25, 26, 29) showed some modest propensity to cluster in the absence of ligand (**Fig. 4e**), which is consistent with roles played by CD28 in T cell signaling at the immunological synapse (43). In general, TMD choice conferred little effect (CD28-TMD) or no effect (all other tested TMDs) on the propensity of MESA chains to associate in the presence or absence of ligand. Thus, there must exist an alternative explanation as to why TMD choice profoundly impacts background signaling, ligand-induced signaling, and even PRS cleavability. We propose that TMDs primarily contribute to receptor performance by influencing the geometry in which intracellular domains interact. Several lines of evidence support this hypothesis. Systematically varying the geometry with which TMDs associate either facilitates or constrains MESA receptor signaling (**Fig. 4f,g**), and some TMDs can render a TC resistant to cleavage by a PC (**Fig. 2c, Supplementary Fig. 8**). TMD-associated trends also held—to some extent—across various choices of ligand and ligand-binding domains (**Fig. 5a–d**). Although it is not yet clear *why* each TMD pair impacts the geometry with which intracellular domains associate, experimentally screening the TMD library reported here enabled the improvement of existing MESA receptors based upon each of two distinct mechanisms (**Fig. 5**) (25, 26, 29). It remains to be seen whether further TMD screening or engineering may represent an opportunity for further performance enhancement of MESA receptors, and whether TMD substitution may improve other synthetic receptors.

Ultimately, we hope that this investigation will serve as a guide for building and tuning synthetic receptors by connecting design choices to biophysical consequences and performance characteristics of interest (**Fig. 6c**). Some choices must be made at the outset; for example, the geometry with which ligand-binding domains are separated in physical space when bound to ligand fundamentally limits inter-chain interactions (**Fig. 6a,b**). Minimizing the apposition of these domains may benefit MESA receptor performance (e.g., rapamycin compared to gibberellin and abscisic acid receptors in **Fig. 5** and **Fig. 6**). Other choices such as TMD selection and expression tuning provide fairly facile handles for optimizing (empirically, if needed) receptor performance characteristics to meet the needs of a given application. The methods and insights developed here should facilitate the construction of novel, high performing receptors for diverse ligands, including both MESA receptors and potentially synthetic receptor systems in general.

DATA AVAILABILITY

Plasmid maps are provided as annotated GenBank files in **Supplementary Data 2**. Plasmids and complete annotated GenBank files will be deposited with Addgene. This study uses Addgene plasmids #58855, #138749 (described in **Materials and Methods**). All reported experimental data will be provided in **Source Data 1 upon final submission in a digital repository**.

FUNDING

This work was supported in part by the National Institute of Biomedical Imaging and Bioengineering of the National Institutes of Health (NIH) under award number 1R01EB026510, the National Cancer Institute (NCI) of the NIH under award number F30CA203325, the National Institute of General Medical Sciences (NIGMS) of the NIH under award number T32GM008152 (to Hossein Ardehali), the National Science Foundation under award number MCB-1745753, the Northwestern University Flow Cytometry Core Facility supported by Cancer Center Support Grant (NCI 5P30CA060553), and the NUSeq Core of the Northwestern Center for Genetic Medicine. Microscopy was performed at the Biological Imaging Facility at Northwestern University, graciously supported by the Chemistry of Life Processes Institute, the NU Office for Research, and the Rice Foundation. The content is solely the responsibility of the authors and does not necessarily represent the official views of the NIH.

REFERENCES

1. Muldoon, J.J., Donahue, P.S., Dolberg, T.B., Leonard, J.N. (2017) Building with intent: technologies and principles for engineering mammalian cell-based therapies to sense and respond. *Curr Opin Biomed Eng,* 4, 127–133.

2. Guedan, S., Ruella, M., June, C.H. (2019) Emerging Cellular Therapies for Cancer. *Annu Rev Immunol,* 37, 145-171.

3. Roybal, K.T., Lim, W.A. (2017) Synthetic Immunology: Hacking Immune Cells to Expand Their Therapeutic Capabilities. *Annu Rev Immunol,* 35, 229-253.

4. Kojima, R., Aubel, D., Fussenegger, M. (2020) Building sophisticated sensors of extracellular cues that enable mammalian cells to work as "doctors" in the body. *Cell Mol Life Sci*.

5. Schwarz, K.A., Leonard, J.N. (2016) Engineering cell-based therapies to interface robustly with host physiology. *Adv Drug Deliv Rev,* 105, 55-65.

6. Chen, L.C., Chen, Y.Y. (2019) Outsmarting and outmuscling cancer cells with synthetic and systems immunology. *Curr Opin Biotechnol,* 60, 111-118.

7. Ishizuka, S. *et al.* (2018) Designing motif-engineered receptors to elucidate signaling molecules important for proliferation of hematopoietic stem cells. *ACS Synth Biol,* 7, 1709-1714.

8. Engelowski, E. *et al.* (2018) Synthetic cytokine receptors transmit biological signals using artificial ligands. *Nat Commun,* 9, 2034.

9. Qudrat, A., Truong, K. (2017) Engineering synthetic proteins to generate Ca(2+) signals in mammalian cells. *ACS Synth Biol,* 6, 582-590.

10. Conklin, B.R. *et al.* (2008) Engineering GPCR signaling pathways with RASSLs. *Nat Methods,* 5, 673-678.

11. Kojima, R., Scheller, L., Fussenegger, M. (2018) Nonimmune cells equipped with T-cell-receptor-like signaling for cancer cell ablation. *Nat Chem Biol,* 14, 42-49.

12. Scheller, L., Strittmatter, T., Fuchs, D., Bojar, D., Fussenegger, M. (2018) Generalized extracellular molecule sensor platform for programming cellular behavior. *Nat Chem Biol,* 14, 723-729.

13. Qudrat, A., Mosabbir, A.A., Truong, K. (2017) Engineered proteins program mammalian cells to target inflammatory disease sites. *Cell Chem Biol,* 24, 703-711 e702.

14. Qudrat, A., Truong, K. (2017) Autonomous cell migration to CSF1 sources via a synthetic protein-based system. *ACS Synth Biol,* 6, 1563-1571.

15. Chung, H.K. *et al.* (2019) A compact synthetic pathway rewires cancer signaling to therapeutic effector release. *Science,* 364.

16. Barnea, G. *et al.* (2008) The genetic design of signaling cascades to record receptor activation. *Proc Natl Acad Sci U S A,* 105, 64-69.

17. Kipniss, N.H. *et al.* (2017) Engineering cell sensing and responses using a GPCR-coupled CRISPR-Cas system. *Nat Commun,* 8, 2212.

18. Maze, A., Benenson, Y. (2020) Artificial signaling in mammalian cells enabled by prokaryotic two-component system. *Nat Chem Biol,* 16, 179-187.

19. Baeumler, T.A., Ahmed, A.A., Fulga, T.A. (2017) Engineering synthetic signaling pathways with programmable dCas9-based chimeric receptors. *Cell Rep,* 20, 2639-2653.

20. Krawczyk, K., Scheller, L., Kim, H., Fussenegger, M. (2020) Rewiring of endogenous signaling pathways to genomic targets for therapeutic cell reprogramming. *Nature Communications,* 11.

21. Morsut, L. *et al.* (2016) Engineering customized cell sensing and response behaviors using synthetic notch receptors. *Cell,* 164, 780-791.

22. Roybal, K.T. *et al.* (2016) Precision tumor recognition by T cells with combinatorial antigen-sensing circuits. *Cell,* 164, 770-779.

23. Roybal, K.T. *et al.* (2016) Engineering T cells with customized therapeutic response programs using synthetic notch receptors. *Cell,* 167, 419-432 e416.

24. Yang, Z., Yu, Z., Cai, Y., Du, R., Cai, L. (2020) Engineering of an enhanced synthetic Notch receptor by reducing ligand-independent activation. *Communications Biology,* 3, 116.

25. Daringer, N.M., Dudek, R.M., Schwarz, K.A., Leonard, J.N. (2014) Modular extracellular sensor architecture for engineering mammalian cell-based devices. *ACS Synth Biol,* 3, 892-902.

26. Dolberg, T.B. *et al.* (2019) Computation-guided optimization of split protein systems. *bioRxiv*.

27. Hartfield, R.M., Schwarz, K.A., Muldoon, J.J., Bagheri, N., Leonard, J.N. (2017) Multiplexing Engineered Receptors for Multiparametric Evaluation of Environmental Ligands. *ACS Synth Biol,* 6, 2042-2055.

28. Brenner, M., Cho, J.H., Wong, W.W. (2017) Synthetic biology: Sensing with modular receptors. *Nat Chem Biol,* 13, 131-132.

29. Schwarz, K.A., Daringer, N.M., Dolberg, T.B., Leonard, J.N. (2017) Rewiring human cellular input-output using modular extracellular sensors. *Nat Chem Biol,* 13, 202-209.

30. Tang, J.C. *et al.* (2013) A nanobody-based system using fluorescent proteins as scaffolds for cell-specific gene manipulation. *Cell,* 154, 928-939.

31. Donahue, P.S. *et al.* (2020) The COMET toolkit for composing customizable genetic programs in mammalian cells. *Nat Commun,* 11, 779.

32. Xia, Z., Liu, Y. (2001) Reliable and global measurement of fluorescence resonance energy transfer using fluorescence microscopes. *Biophys J,* 81, 2395-2402.

33. Zal, T., Gascoigne, N.R. (2004) Photobleaching-corrected FRET efficiency imaging of live cells. *Biophys J,* 86, 3923-3939.

34. Liang, J., Choi, J., Clardy, J. (1999) Refined structure of the FKBP12-rapamycin-FRB ternary complex at 2.2 A resolution. *Acta Crystallogr D Biol Crystallogr,* 55, 736-744.

35. Murase, K., Hirano, Y., Sun, T.P., Hakoshima, T. (2008) Gibberellin-induced DELLA recognition by the gibberellin receptor GID1. *Nature,* 456, 459-463.

36. Yin, P. *et al.* (2009) Structural insights into the mechanism of abscisic acid signaling by PYL proteins. *Nat Struct Mol Biol,* 16, 1230-1236.

37. Fuh, G. *et al.* (2006) Structure-function studies of two synthetic anti-vascular endothelial growth factor Fabs and comparison with the Avastin Fab. *J Biol Chem,* 281, 6625-6631.

38. Dougherty, W., Cary, S.M., Parks, T.D. (1989) Molecular genetic analysis of a plant virus polyprotein cleavage sequence: a model. *Virology,* 171, 356–364.

39. Kapust, R.B. *et al.* (2001) Tobacco etch virus protease: mechanism of autolysis and rational design of stable mutants with wild-type catalytic proficiency. *Protein Eng,* 14, 993-1000.

40. Kapust, R.B., Tozser, J., Copeland, T.D., Waugh, D.S. (2002) The P1' specificity of tobacco etch virus protease. *Biochem Biophys Res Commun,* 294, 949-955.

41. Nunn, C.M. *et al.* (2005) Crystal structure of tobacco etch virus protease shows the protein C terminus bound within the active site. *J Mol Biol,* 350, 145–155.

42. Biggs, M.J., Milone, M.C., Santos, L.C., Gondarenko, A., Wind, S.J. (2011) High-resolution imaging of the immunological synapse and T-cell receptor microclustering through microfabricated substrates. *J R Soc Interface,* 8, 1462-1471.

43. Yokosuka, T., Saito, T. (2009) Dynamic regulation of T-cell costimulation through TCR-CD28 microclusters. *Immunol Rev,* 229, 27-40.

44. Westerfield, J.M., Barrera, F.N. (2020) Membrane receptor activation mechanisms and transmembrane peptide tools to elucidate them. *J Biol Chem,* 295, 1792-1814.

45. Finger, C., Escher, C., Schneider, D. (2009) The single transmembrane domains of human receptor tyrosine kinases encode self-interactions. *Sci Signal,* 2, ra56.

46. Alabanza, L. *et al.* (2017) Function of Novel Anti-CD19 Chimeric Antigen Receptors with Human Variable Regions Is Affected by Hinge and Transmembrane Domains. *Mol Ther,* 25, 2452-2465.

47. Bridgeman, J.S. *et al.* (2010) The optimal antigen response of chimeric antigen receptors harboring the CD3zeta transmembrane domain is dependent upon incorporation of the receptor into the endogenous TCR/CD3 complex. *J Immunol,* 184, 6938-6949.

48. Chen, L.I., Webster, M.K., Meyer, A.N., Donoghue, D.J. (1997) Transmembrane domain sequence requirements for activation of the p185c-neu receptor tyrosine kinase. *J Cell Biol,* 137, 619-631.

49. Lomize, A.L., Pogozheva, I.D. (2017) TMDOCK: An Energy-Based Method for Modeling alpha-Helical Dimers in Membranes. *J Mol Biol,* 429, 390-398.

50. Banning, C. *et al.* (2010) A flow cytometry-based FRET assay to identify and analyse protein-protein interactions in living cells. *PLoS One,* 5, e9344.

51. Goedhart, J. *et al.* (2010) Bright cyan fluorescent protein variants identified by fluorescence lifetime screening. *Nat Methods,* 7, 137-139.

52. Day, R.N., Davidson, M.W. (2009) The fluorescent protein palette: tools for cellular imaging. *Chem Soc Rev,* 38, 2887-2921.

53. Doura, A.K., Fleming, K.G. (2004) Complex interactions at the helix-helix interface stabilize the glycophorin A transmembrane dimer. *J Mol Biol,* 343, 1487-1497.

54. Koushik, S.V., Chen, H., Thaler, C., Puhl, H.L., 3rd, Vogel, S.S. (2006) Cerulean, Venus, and VenusY67C FRET reference standards. *Biophys J,* 91, L99-L101.

55. Berney, C., Danuser, G. (2003) FRET or no FRET: a quantitative comparison. *Biophys J,* 84, 3992-4010.

56. Bell, C.A. *et al.* (2000) Rotational coupling of the transmembrane and kinase domains of the Neu receptor tyrosine kinase. *Mol Biol Cell,* 11, 3589-3599.

57. Kirchhofer, A. *et al.* (2010) Modulation of protein properties in living cells using nanobodies. *Nat Struct Mol Biol,* 17, 133-138.

58. Gao, Y. *et al.* (2016) Complex transcriptional modulation with orthogonal and inducible dCas9 regulators. *Nat Methods,* 13, 1043-1049.

59. Algar, W.R., Hildebrandt, N., Vogel, S.S., Medintz, I.L. (2019) FRET as a biomolecular research tool - understanding its potential while avoiding pitfalls. *Nat Methods,* 16, 815-829.

60. Chan, F.K. *et al.* (2000) A domain in TNF receptors that mediates ligand-independent receptor assembly and signaling. *Science,* 288, 2351-2354.

61. Hochreiter, B., Garcia, A.P., Schmid, J.A. (2015) Fluorescent proteins as genetically encoded FRET biosensors in life sciences. *Sensors (Basel),* 15, 26281-26314.

ACKNOWLEDGEMENTS

The authors would like to thank Stephen Lander and Simrita Deol for assistance with some of the experiments and data analysis, Cameron McDonald for assistance with the PC mutagenesis study, the Neha Kamat lab for use of an Azure c280 imager, and members of the Leonard lab for useful discussions.

AUTHOR CONTRIBUTIONS

H.I.E., P.S.D., J.J.M., T.B.D., and J.N.L. conceived and designed this study. H.I.E., P.S.D., J.J.M., A.K., T.B.D., L.M.B., E.R.A, and M.H. generated reagents. H.I.E., P.S.D., J.J.M., A.K., T.B.D., L.M.B., and E.R.A. designed and performed experiments and analyzed the data. H.I.E., P.S.D., J.J.M., and J.N.L. wrote the manuscript, and all authors edited and approved the final manuscript.

COMPETING INTERESTS

J.N.L. is an inventor on related intellectual property: United States Patent 9,732,392; WO2013022739.

FIGURES

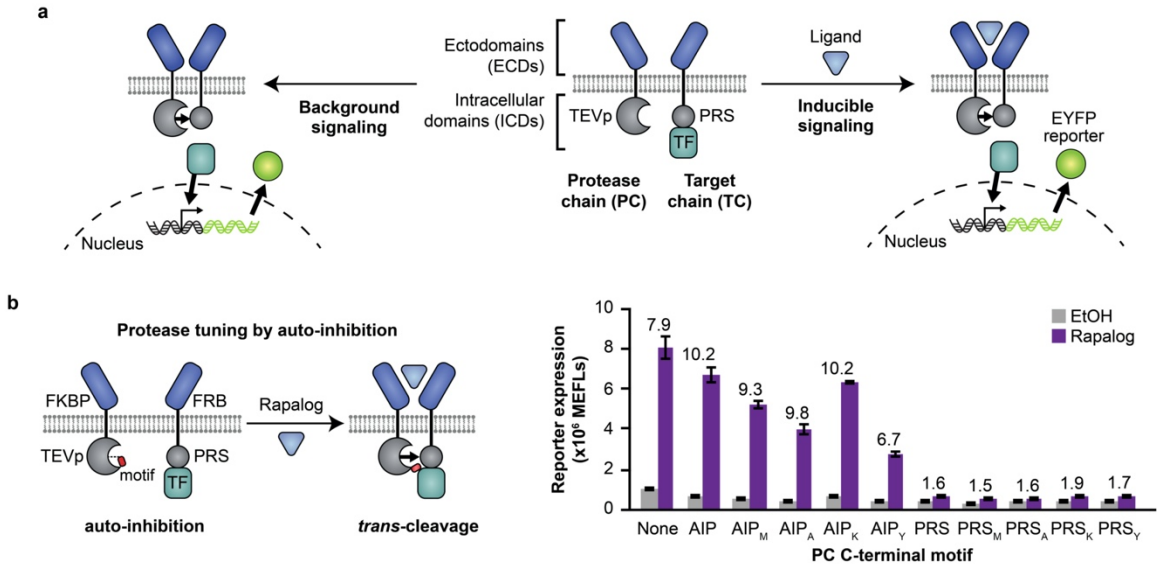

Fig. 1 Protease chain tuning to improve MESA receptor performance. a This schematic depicts the MESA signaling mechanism. Ligand-induced receptor dimerization results in TEVp-mediated *trans*-cleavage to release a TF, which then enters the nucleus and induces target gene expression (right). Ligand-independent (background) receptor interactions can also result in TF release (left). **b** Functional assay for MESA receptor variants with a modified AIP (ELVYSQX) or PRS (ENLYFQX), where X is a variable amino acid, appended onto the C-terminus of the PC TEVp. The leftmost condition is the base case (no appended motif). Each condition uses a TC with M at the P1' site of the PRS. Bars depict the mean of three biologic replicates, and error bars represent the S.E.M. Numbers above bars indicate fold difference (F.D.) in reporter signal between samples treated with rapalog (dissolved in EtOH) vs. EtOH (vehicle-only control).

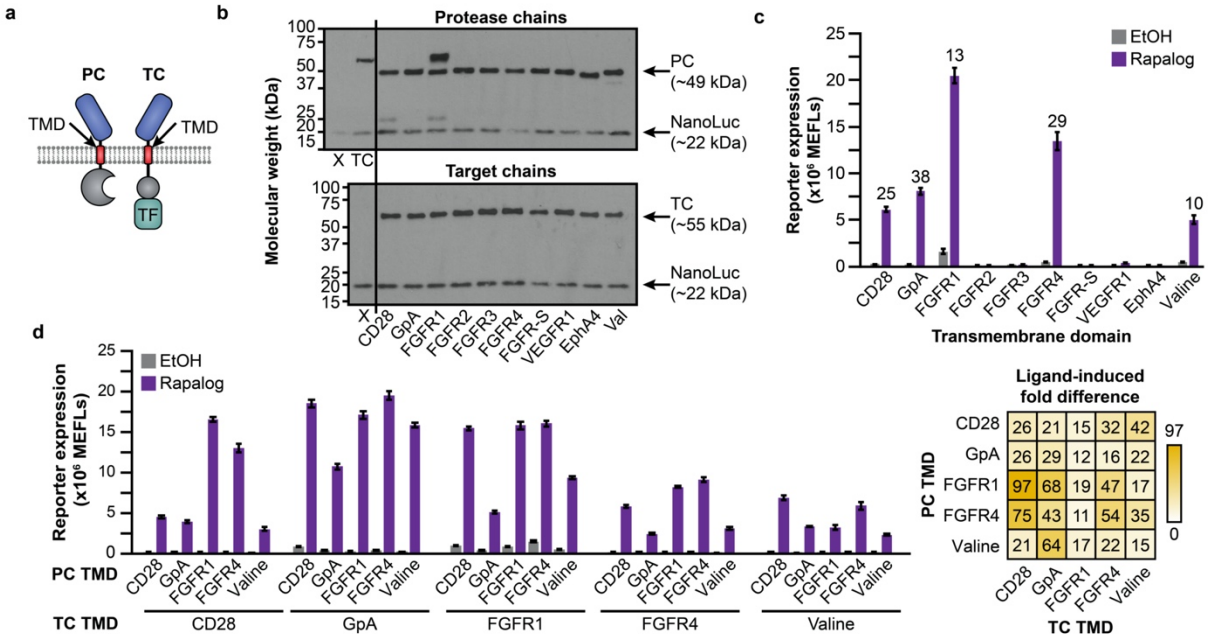

Fig. 2 TMD contributions to MESA receptor signaling. a This schematic identifies the design choice examined here—the TMD sequence. **b** Effect of TMD choice on the expression of expected bands (PC, TC, co-transfected NanoLuc loading control) versus cleavage products (CD28 and FGFR1 cases). For this experiment, chain expression levels were first normalized to that of CD28-TMD TC expression (M, upper panel) by varying transfected plasmid dose through iterative Western blot analyses (**Supplementary Fig. 6**). The X denotes a vector-only negative control (including NanoLuc); TC denotes a CD28-TMD TC. **c** Paired TMD substitution conferred varying effects on receptor performance. Numbers above bars indicate F.D. when ligand induced significant signal above background ($p < 0.05$). **d** Combinatorial TMD substitution further improved receptor performance. F.D. is reported in the heatmap at right. All combinations exhibit a significant increase in reporter expression upon ligand treatment (three-factor ANOVA, $p < 0.001$). Bars depict the mean of three biologic replicates, and error bars represent the S.E.M. Outcomes from ANOVAs and Tukey's HSD tests for **c,d** are in **Supplementary Notes 1 and 2**.

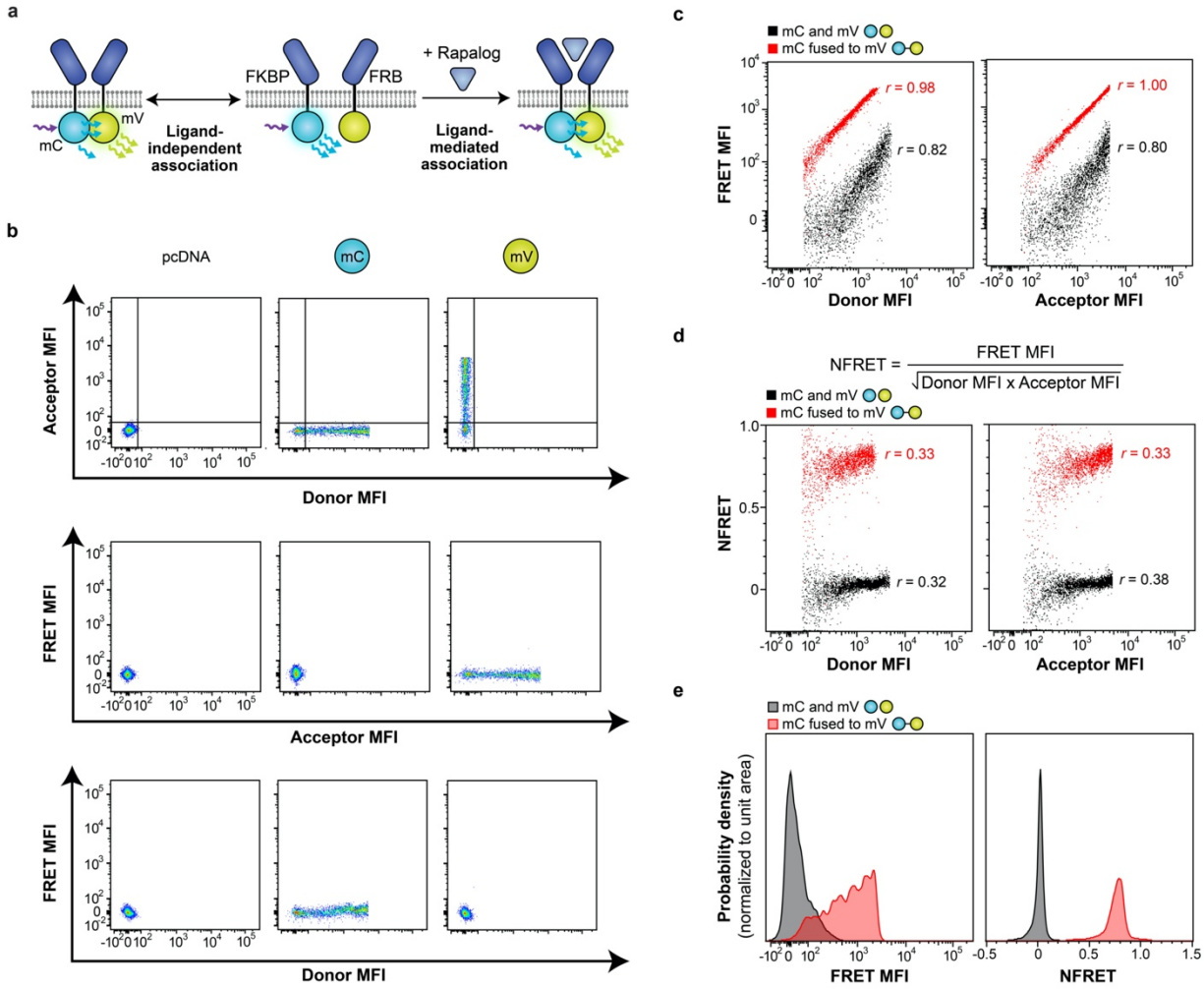
a
mC
mV
Ligand-independent association
FKBP
FRB
+ Rapalog
Ligand-mediated association
b
pcDNA
mC
mV
Acceptor MFI
Donor MFI
FRET MFI
Acceptor MFI
FRET MFI
Donor MFI
c
mC and mV
mC fused to mV
r = 0.98
r = 0.82
r = 1.00
r = 0.80
FRET MFI
Donor MFI
Acceptor MFI
d
NFRET = FRET MFI / √(Donor MFI x Acceptor MFI)
mC and mV
mC fused to mV
r = 0.33
r = 0.32
r = 0.33
r = 0.38
NFRET
Donor MFI
Acceptor MFI
e
mC and mV
mC fused to mV
Probability density (normalized to unit area)
FRET MFI
NFRET

Fig. 3 Development of a flow cytometric FRET approach to probe receptor chain association. a This schematic illustrates our strategy for quantifying ligand-independent (left) and ligand-mediated (right) receptor associations using Förster resonance energy transfer (FRET). Rapamycin-sensing MESA receptor ICDs were replaced with mCerulean (donor) and mVenus (acceptor) fluorophores. **b** Single-fluorophore samples were used to linearly compensate bleed-through from individual fluorophores into both the other fluorophore channel and the FRET channel. These plots also illustrate the gating used to identify cells expressing both the donor and acceptor fluorophores (mCerulean+/mVenus+). **c** Cytosolically expressed control constructs that are expected to display low FRET (separate soluble donor and acceptor proteins) or high FRET (donor-acceptor fusion protein) differ by a vertical shift in fluorescence in the FRET channel. Fluorescence in the FRET channel is linearly correlated with donor and acceptor fluorescence, respectively. The cells shown are singlets that are transfected (mIRFP670+) and that express the donor and acceptor (mCerulean+/mVenus+). **d** When FRET fluorescence is normalized to donor and acceptor fluorescence intensities by the calculated NFRET metric (equation shown), the cytosolic controls still display a vertical shift in NFRET, but NFRET only has a low correlation with donor and acceptor fluorescence, respectively; NFRET is more independent of expression differences observed across the cell population (compared to FRET MFI in **c**). The cells shown are singlets that are transfected (mIRFP670+) and that express the donor and acceptor (mCerulean+/mVenus+). **e** The NFRET metric better distinguishes low and high FRET controls than does unprocessed FRET fluorescence. Experiments were conducted in biologic triplicate, and individual representative samples are shown. Data were analyzed as described in **Methods**.

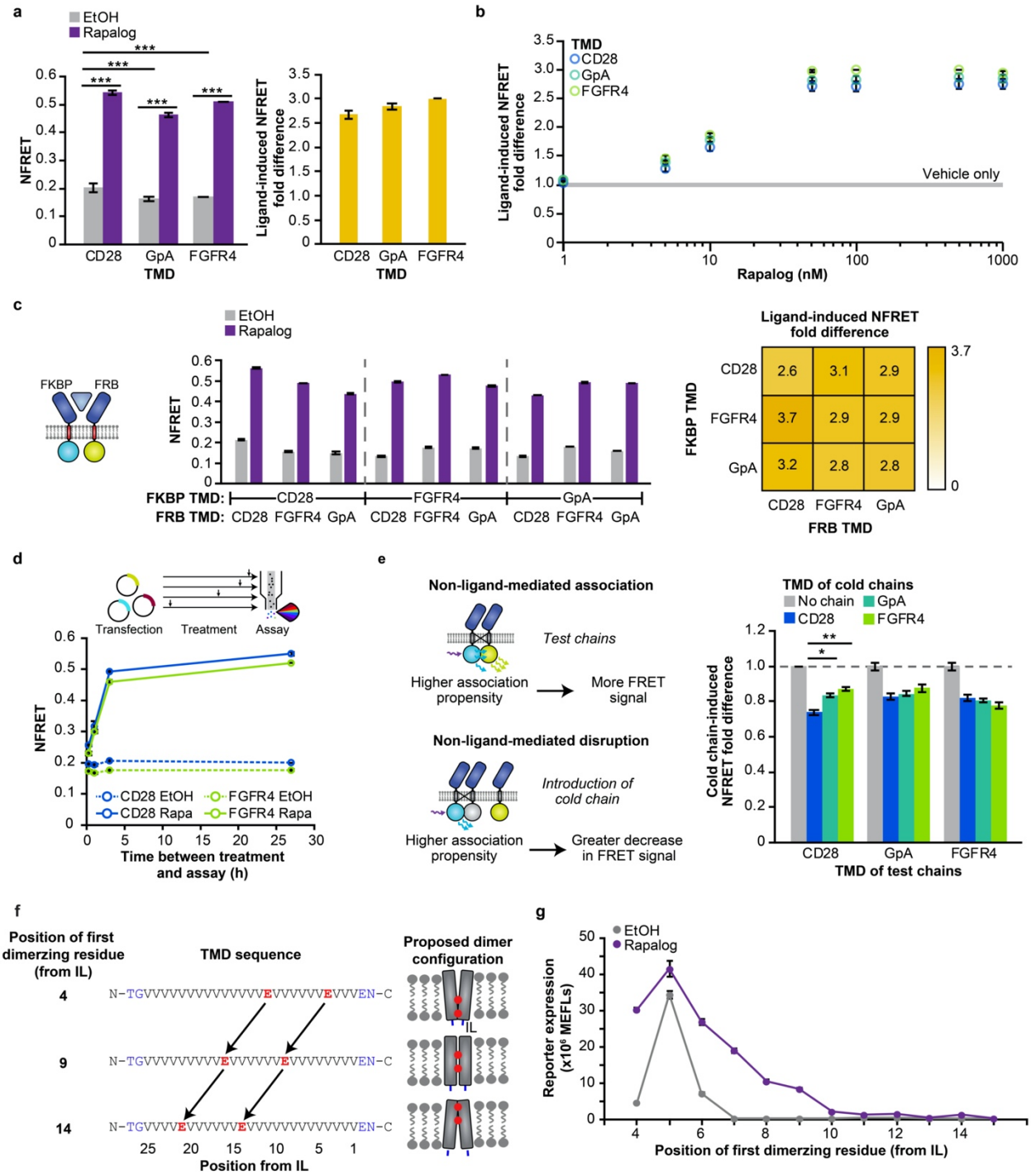
a
EtOH
Rapalog
NFRET
CD28
GpA
FGFR4
TMD
Ligand-induced NFRET fold difference
b
TMD
CD28
GpA
FGFR4
Vehicle only
Rapalog (nM)
c
FKBP
FRB
FKBP TMD:
FRB TMD:
Ligand-induced NFRET fold difference
FKBP TMD
FRB TMD
d
Transfection
Treatment
Assay
CD28 EtOH
CD28 Rapa
FGFR4 EtOH
FGFR4 Rapa
Time between treatment and assay (h)
e
Non-ligand-mediated association
Test chains
Higher association propensity
More FRET signal
Non-ligand-mediated disruption
Introduction of cold chain
Greater decrease in FRET signal
TMD of cold chains
No chain
Cold chain-induced NFRET fold difference
TMD of test chains
f
Position of first dimerzing residue (from IL)
TMD sequence
Proposed dimer configuration
Position from IL
g
Reporter expression (x10⁶ MEFLs)
Position of first dimerzing residue (from IL)

Fig. 4 Effect of TMD choice on receptor chain association. a Receptor pairs with matched TMDs exhibit a ligand-induced increase in NFRET (27 h incubation, 100 nM rapalog) (two-factor ANOVA, ***$p < 0.001$) (left). The CD28-TMD matched receptor pair exhibits slightly higher NFRET in the absence of ligand compared to the GpA-TMD pair and FGFR4-TMD pair (two-factor ANOVA, ***$p < 0.001$). Fractional change in NFRET upon ligand treatment (ligand-induced NFRET fold difference) is comparable across TMDs (two-tailed Welch's *t*-test, all $p > 0.05$) (right). In all cases, the donor fluorophore is on the FKBP chain and the acceptor fluorophore is on the FRB chain. **b** NFRET induction varies with rapalog dose (measurement at 27 h incubation). **c** Pairs of transfected receptors with mixed and matched TMDs exhibit a significant ligand-induced increase in NFRET (27 h incubation, 100 nM rapalog) (three-factor ANOVA, $p < 0.001$). The ligand-induced NFRET increase is comparable across mixed and matched TMD pairs. **d** Dynamics of NFRET response to ligand. By 3 h post-ligand treatment, the NFRET increase is nearly maximal (87% relative to the NFRET at 27 h). Abbreviation: rapa, rapalog. **e** In a cold (non-fluorescent) chain competition assay with matched TMD fluorescent receptors, CD28-TMD exhibited a slightly higher propensity to associate: the NFRET decrease conferred by introduction of a CD28-TMD cold chain was greater in the CD28-TMD matched case than in other cases (two-tailed Welch's *t*-test, all $p > 0.05$ except for comparison between CD28-mediated and GpA-mediated disruption of CD28 FRET and CD28-mediated vs. FGFR4-mediated disruption of CD28 FRET, *$p < 0.05$, **$p < 0.01$). All chains contain the same ECD (FRB). **f-g** The use of synthetic TMDs with dimerizing residues positioned at different locations in the alpha helix conferred highly varied effects on background and ligand-induced signaling. Juxtamembrane N-terminal outer linker and C-terminal inner linker (IL) residues are shown in blue. Experiments were conducted in biologic triplicate, and data were analyzed as described in **Methods**. Error bars represent the S.E.M. Outcomes from ANOVAs and Tukey's HSD tests for **a–c** are in **Supplementary Notes 1 and 2**.

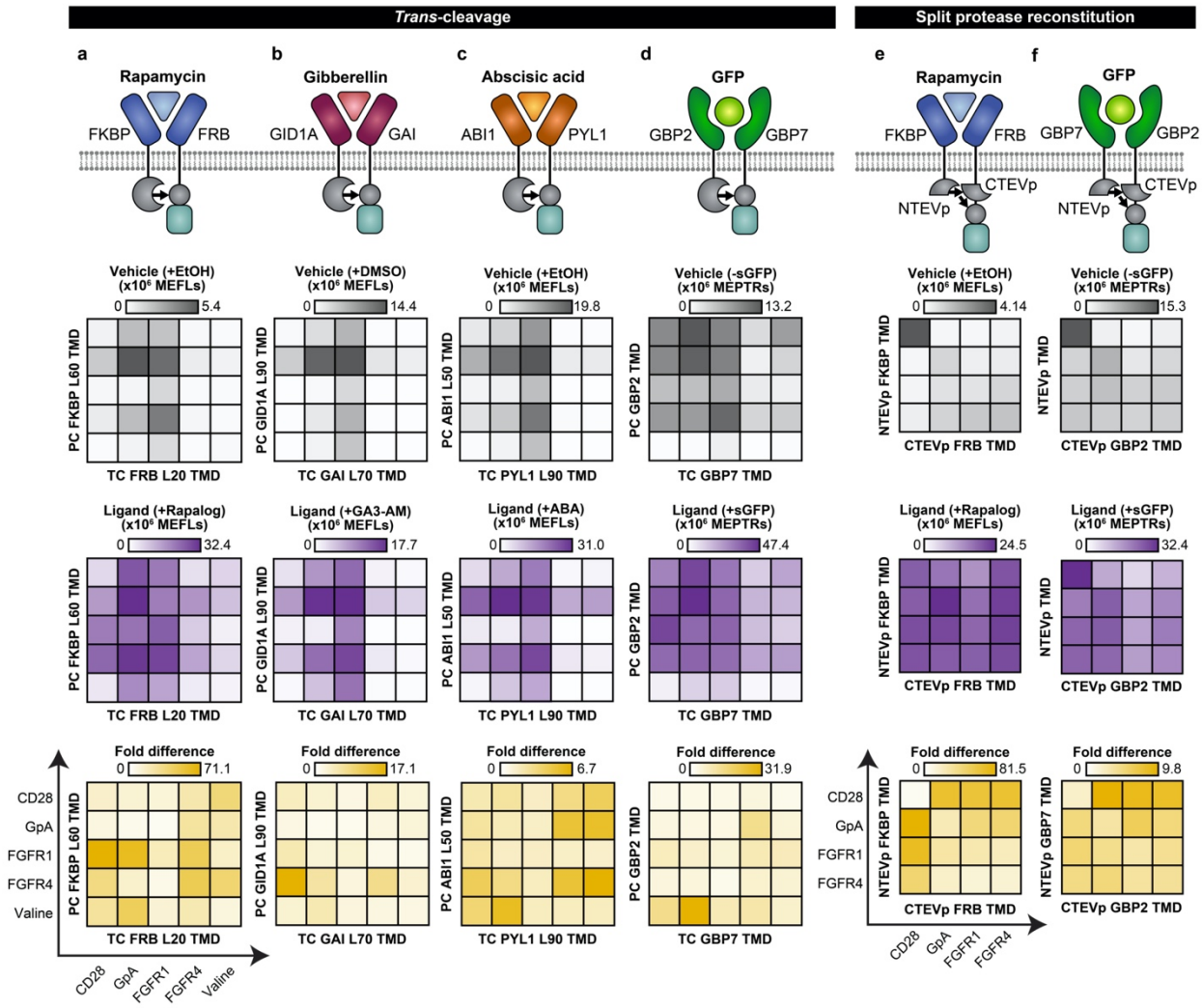
Trans-cleavage
Split protease reconstitution
a
Rapamycin
FKBP
FRB
b
Gibberellin
GID1A
GAI
c
Abscisic acid
ABI1
PYL1
d
GFP
GBP2
GBP7
e
Rapamycin
FKBP
FRB
CTEVp
NTEVp
f
GFP
GBP7
GBP2
CTEVp
NTEVp
Vehicle (+EtOH) (x10⁶ MEFLs)
0 5.4
PC FKBP L60 TMD
TC FRB L20 TMD
Vehicle (+DMSO) (x10⁶ MEFLs)
0 14.4
PC GID1A L90 TMD
TC GAI L70 TMD
Vehicle (+EtOH) (x10⁶ MEFLs)
0 19.8
PC ABI1 L50 TMD
TC PYL1 L90 TMD
Vehicle (-sGFP) (x10⁶ MEPTRs)
0 13.2
PC GBP2 TMD
TC GBP7 TMD
Vehicle (+EtOH) (x10⁶ MEFLs)
0 4.14
NTEVp FKBP TMD
CTEVp FRB TMD
Vehicle (-sGFP) (x10⁶ MEPTRs)
0 15.3
NTEVp TMD
CTEVp GBP2 TMD
Ligand (+Rapalog) (x10⁶ MEFLs)
0 32.4
PC FKBP L60 TMD
TC FRB L20 TMD
Ligand (+GA3-AM) (x10⁶ MEFLs)
0 17.7
PC GID1A L90 TMD
TC GAI L70 TMD
Ligand (+ABA) (x10⁶ MEFLs)
0 31.0
PC ABI1 L50 TMD
TC PYL1 L90 TMD
Ligand (+sGFP) (x10⁶ MEPTRs)
0 47.4
PC GBP2 TMD
TC GBP7 TMD
Ligand (+Rapalog) (x10⁶ MEFLs)
0 24.5
NTEVp FKBP TMD
CTEVp FRB TMD
Ligand (+sGFP) (x10⁶ MEPTRs)
0 32.4
NTEVp TMD
CTEVp GBP2 TMD
Fold difference
0 71.1
CD28
GpA
FGFR1
FGFR4
Valine
PC FKBP L60 TMD
TC FRB L20 TMD
Fold difference
0 17.1
PC GID1A L90 TMD
TC GAI L70 TMD
Fold difference
0 6.7
PC ABI1 L50 TMD
TC PYL1 L90 TMD
Fold difference
0 31.9
PC GBP2 TMD
TC GBP7 TMD
Fold difference
0 81.5
CD28
GpA
FGFR1
FGFR4
NTEVp FKBP TMD
CTEVp FRB TMD
Fold difference
0 9.8
NTEVp GBP7 TMD
CTEVp GBP2 TMD

Fig. 5 Tuning an expanded panel of MESA receptor systems. a–d Functional assays for MESA receptors for sensing rapamycin, gibberellin, abscisic acid, and sGFP were constructed using the full TEVp-based *trans*-cleavage mechanism. **e,f** Functional assays for MESA receptors for sensing rapamycin and sGFP were constructed using a revised mechanism, including previously reported H75S/L190K mutations for tuning split TEVp reconstitution propensity (26). ECDs and extracellular linker lengths are unique to each set of ligand-binding domains (**Supplementary Figs. 21, 23**). Heatmaps display the mean from three biologic replicates of reporter expression with vehicle only (gray), reporter expression with ligand (purple), and ligand-induced F.D. (gold). Within each system, a consistent plasmid dose was used across conditions. Colors are scaled for each heatmap. Corresponding bar graphs are in **Supplementary Figs. 22, 24, 27–30**). Data were analyzed as described in **Methods**. Outcomes from ANOVAs and Tukey's HSD tests are in **Supplementary Notes 1 and 2**.

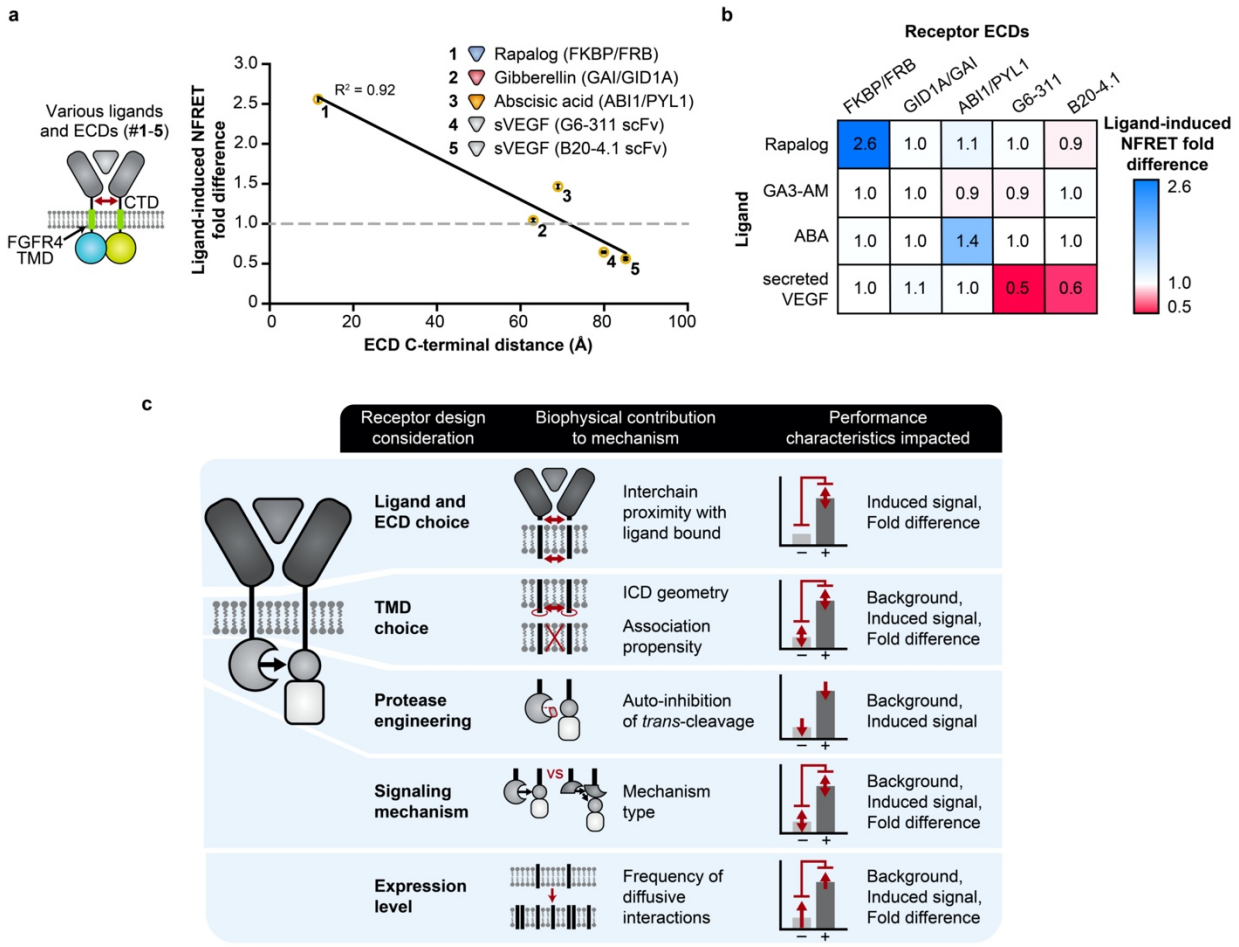

Fig. 6 Generalizing principles for receptor engineering. a Ligand-induced inter-chain association (NFRET fold difference) varies with ECD C-terminal distance, with a negative linear relationship ($y = -0.027x + 2.9$, where y is NFRET fold difference and x is C-terminal distance in Å, $R^2 = 0.92$, two-tailed student's t-test, $p = 0.01$). The ligands are rapalog, GA3-AM, ABA, and secreted VEGF. **b** Validation of orthogonality between ligand and ECD pairs. **c** This schematic summarizes the findings of this investigation by relating receptor design choices to the proposed biophysical consequences and the affected receptor performance characteristics.